DNA adsorption at functionalized Si/buffer interfaces studied by x-ray reflectivity

C. Douarche,[1,2,3] R. Cortès,[1] C. Henry de Villeneuve,[1] S. J. Roser,[4] and A. Braslau[5,a)]
[1]*Physique de la Matière Condensée, École Polytechnique, CNRS, 91128 Palaiseau, France*
[2]*Service de Biologie Intégrative et de Génétique Moléculaire, CEA/Saclay, 91191 Gif-sur-Yvette Cedex, France*
[3]*Institut de Recherche Interdisciplinaire, Cité Scientifique, Avenue Poincaré BP 60069, 59652 Villeneuve d'Ascq Cedex, France*
[4]*Department of Chemistry, University of Bath, Bath, Avon BA2 7AY, United Kingdom*
[5]*Service de Physique de l'État Condensé, CNRS URA 2464, Institut Rayonnement Matière Saclay, CEA/Saclay, 91191 Gif-sur-Yvette Cedex, France*

(Received 7 December 2007; accepted 21 April 2008; published online 13 June 2008)

The adsorption of DNA on chemically homogeneous, functionalized, oxide-free single-crystal silicon surfaces is studied by x-ray reflectivity. The adsorption of monodisperse, 294 base-pair double-stranded DNA on a positively charged surface is detected through the deformation of the molecular monolayer of aminated alkyl-chain molecules covalently bonded to the surface. The adsorption of single-stranded DNA does not lead to the same deformation. A detailed quantitative characterization of the density profiles yield surface densities of the covalently grafted, molecular monolayers that are in excellent agreement with infrared spectroscopic measurements. The additional mass density that is measured following the adsorption of DNA corresponds either to the partial embedding of a densely-packed adsorbed layer or to a deeper penetration into the soft surface layer at a lower surface density of the adsorbed double-stranded DNA molecules. The adsorption is found to be irreversible under high added salt concentrations, suggesting a partial dehydration of the double-stranded DNA. © *2008 American Institute of Physics*. [DOI: 10.1063/1.2927256]

I. INTRODUCTION

How does DNA adsorb from solution onto solid interfaces? The initial interest in this question was concerned with the development of techniques to visualize the DNA macromolecules by electron microscopy[1–5] and, later, without the use of contrast-enhancing masking techniques, by scanning tunneling microscopy,[6–9] and by atomic force microscopy (AFM).[8,10–17] The immobilization of nucleic acids, polynucleotides, oligonucleotides, or nucleic acid residues on a stationary phase followed by specific and reversible base pairing, used for the separation and isolation of nucleic acids and their fragments, is a particular type of affinity chromatography.[18] The immobilization of nucleic acids is also used in many other hybridization techniques. For example, multiplexing approaches to DNA sequencing[19] have found biotechnological applications as hybridization biochips or microarrays.[20–22]

From a more fundamental point of view, Rhodes and Klug[23] used the adsorption of double-stranded DNA on three different, flat surfaces in a very ingenious technique to determine the solution helical periodicity of DNA by enzymatic digestion, probing the accessibility of the phosphodiester bonds. More generally, the interaction of the genetic material with its environment, i.e., the interaction of DNA with proteins, can be thought of in terms of adsorption on the surface of the proteins themselves, with membranes or with the cellular envelopes. Thus, the adsorption of DNA at interfaces, in particular, with "soft" surfaces, is of enormous biological interest.

Furthermore, biochemical processes such as DNA hybridization can be greatly accelerated by the reduction of dimensionality[24] when adsorbed at interfaces.[25] A source of efficiency *in vivo*, this property can also be exploited advantageously in biotechnological devices and is, thus, of great practical importance. The manipulation of a multiphase fluid system in a microfluidic device[26] is only possible in the presence of containers or substrates. This involves, therefore, liquid-solid interfaces, the chemistry of which must be controlled. In the present work, we looked to produce and characterize very chemically pure solid surfaces, positively charged, and to study the phenomenon of DNA adsorption under these conditions. A main result is that the adsorption of double-stranded DNA on a functionalized solid surface leads to the deformation of the covalently bonded organic surface layer.

In the next section, we will describe the surface chemistry developed in order to produce clean, functionalized substrates and their characterization by AFM. We then detail the *in situ* technique of x-ray reflectivity. Preliminary measurements were performed via an energy-dispersive technique using a sealed-tube laboratory x-ray source followed by fixed-wavelength reflectivity measurements using a third-generation synchrotron radiation source. Details of the measurement scheme are described, in particular, concerning the minimization of the contribution of surface-diffuse scattering

a)Author to whom correspondence should be addressed. Electronic mail: alan.braslau@cea.fr.

via tight instrumental resolution and the systematic recording of "rocking curves" around the specular condition. The question of surface degradation under irradiation is addressed, measured, and then controlled. The functionalized surfaces are then characterized quantitatively both in air and under aqueous buffer. Finally, the adsorption of double-stranded DNA is observed, in contrast to single-stranded DNA, which does not penetrate and deform the grafted, dense organic molecular monolayer.

II. FUNCTIONALIZATION OF SILICON SURFACES

Single-crystal silicon surfaces were modified through the covalent grafting of a molecular monolayer functionalized by terminal amine groups in order to investigate the electrostatic immobilization of DNA. Single-crystal silicon is a substrate material of choice. Its surface chemistry is well controlled[27] and its topography is well-defined. Large, flat, very smooth surfaces can be obtained.

In this work, Si(111) wafers[28] were first cleaned in a "piranha" solution ($1\cdot H_2O_2:2\cdot H_2SO_4$), then stripped of their native oxide layer by anisotropic etching in an ammonium fluoride (NH_4F) bath (pH 7–8). This chemical reaction[29,30] removes the surface oxide down to the Si(111) dense planes, yielding a stairway of regular, monoatomic steps when the miscut is oriented in the crystallographic $[11\bar{2}]$ direction[31,32] (see Fig. 1). Through a multistep chemical process (see Fig. 2), a covalently bonded functionalized molecular monolayer is then grafted[33] (that also protects the hydrogenated bare silicon surface against oxidation). First, an ester terminated alkyl chain, ethyl undecylenate $[CH_2{=}CH{-}(CH_2)_8{-}CO{-}O{-}C_2H_5]$ is covalently attached to the silicon crystal lattice via a thermally activated hydrosilylation reaction. The ester is hydrolyzed into a carboxylic acid group, allowing the subsequent coupling [via a N-hydroxysuccinimide ester (NHS)] to an amine group of various molecules, yielding the desired chemical functionalization of the organic layer. An aminated surface that can be made positively charged under buffer can be obtained through the attachment of ethylenediamine ($NH_2{-}CH_2{-}CH_2{-}NH_2$) (see Fig. 3). However, we note that the NHS coupling is incomplete as estimated by surface infrared spectroscopy,[33] so the terminal functionalization will be mixed.

The resulting monolayer is covalently bonded to the single-crystal silicon substrate. As the Si—C bond is oriented in the crystallographic (111) direction and the lines joining successive carbon atoms are inclined according to the tetrahedral angle of 109°28′, the average backbone would adopt a tilt angle of 35°16′. A molecular-scale model representation of the dense monomolecular layer is drawn in Fig. 4.

Throughout this multistep chemical process of functionalization, the atomically flat crystalline structure of the original etched silicon surface can be preserved. AFM images of the stripped and ethylenediamine functionalized surfaces are shown in Fig. 5. Whereas each step terrace is, indeed, atomically flat in these substrates, for each image, the numerically calculated root-mean-squared roughnesses $\langle z^2\rangle^{1/2}$ depends on

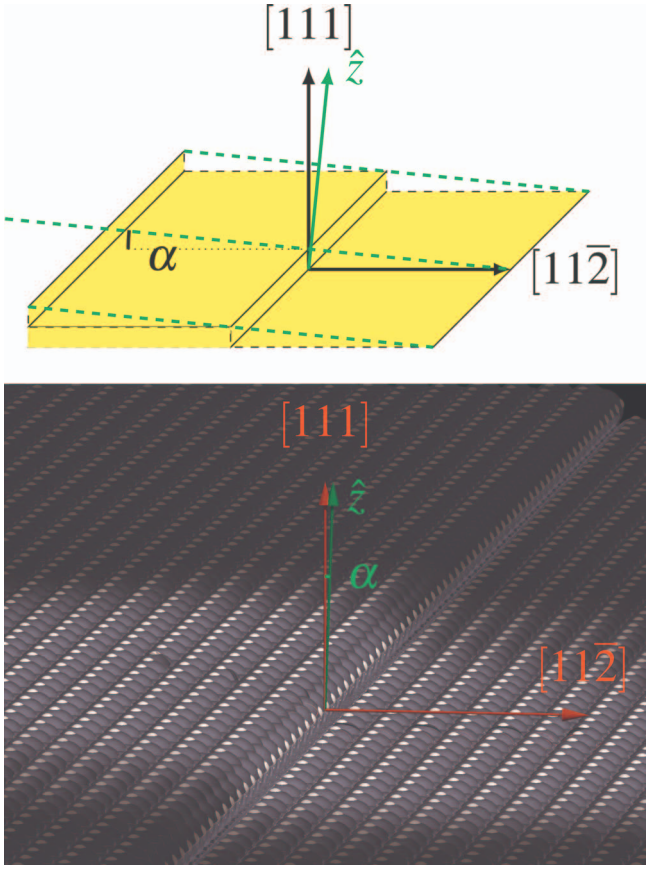

FIG. 1. (Color) Si(111). A miscut of angle α in the $[11\bar{2}]$ direction between the macroscopic surface-normal unit-vector $\hat{z}$ and the [111] direction yields a surface of dense atomic planes with regular steps of height $d_{(111)}=0.314$ nm and width $\ell=d_{(111)}/\tan\alpha$. Top: Schema and bottom: Hydrogen-terminated, atomic-scale model.

the image scale, yielding 0.155 nm rms over 2×2 μm^2 (0.148 nm rms over 1×1 μm^2 and 0.144 nm rms over 500×500 nm^2, not shown) for the amine-terminated monolayer surface. For a simple, one-dimensional steplike interface, $z(x)=d_{(111)}x/\ell\,[0,\ell]$ and the roughness is

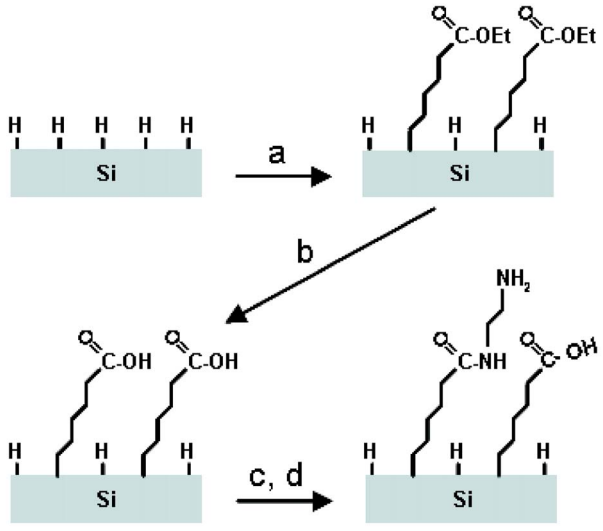

FIG. 2. (Color online) Multistep protocol for the covalent anchoring of an amine-functionalized molecular monolayer on a Si—H surface. (a) Grafting of ester-functionalized alkyl chains, (b) hydrolysis of ester groups, and [(c) and (d)] activation of acid groups and coupling of ethyldiamine.

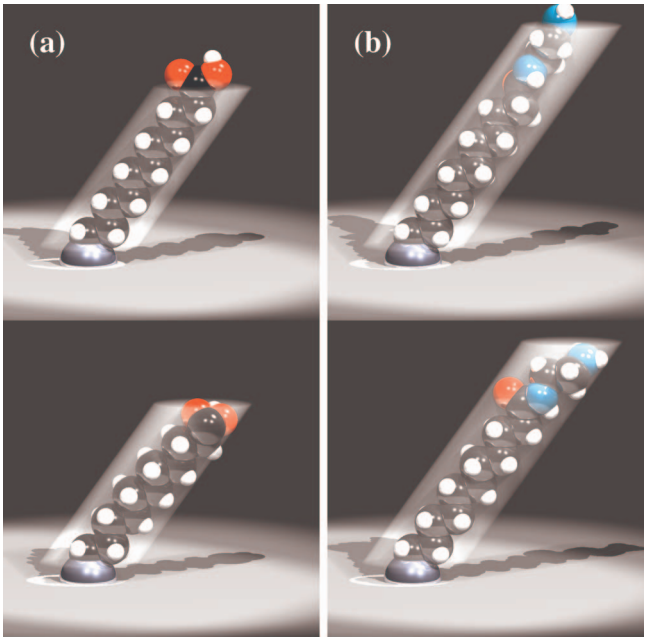

FIG. 3. (Color) Molecular models of (a) dodecanoic acid and (b) dodecanamide, *N*-(2-aminoethyl) (with a surface silicon atom of the crystalline lattice replacing the terminal methyl groups). Fully extended (top) and disordered (bottom) conformations. Red. oxygen, blue: Nitrogen, black: Carbon and white: Hydrogen. The cylinders represent volumes of 0.278×1.085 and 0.294×1.504 nm^2, respectively, occupied on average by each molecule, as determined by the x-ray reflectivity measurements (Sec. III B).

$$\langle z^2\rangle^{1/2}=\left\{\frac{1}{\ell}\int_0^{\ell}dx[z(x)-\langle z\rangle]^2\right\}^{1/2}$$
$$=\frac{d_{(111)}}{2\ell}\left(\frac{1}{\ell}\int_0^{\ell}dx\cdot x^2\right)^{1/2}=\frac{d_{(111)}}{2\sqrt{3}}=0.091\ \text{nm}. \quad (1)$$

The discrete AFM roughness, therefore, overestimates the expected value. Note that the AFM technique, in contrast to x-ray scattering, does not take into account atomic-scale roughness (R_{Si}=0.11 nm); the root-mean-squared roughness over all lateral length scales including both the atomic-plane steps and atomic discreetness is expected to be on the order of $\sqrt{0.091^2+0.11^2}=0.14$ nm.

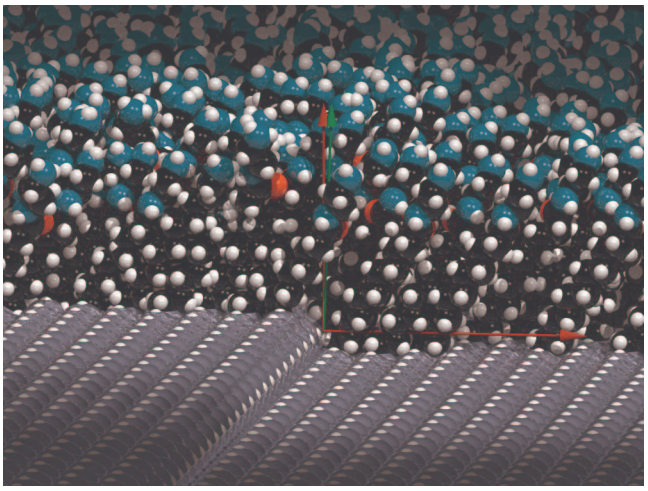

FIG. 4. (Color) Molecular-scale model representation of the functionalized silicon surface. Red: Oxygen, blue: Nitrogen, black: Carbon, and white: Hydrogen. The model is drawn with a random surface coverage of 44% of the available Si—H bonding sites [and an *arbitrarily* chosen in-plane nematic order parameter for the azimuthal carbon-chain tilt direction β of $S=\langle\frac{1}{2}(3\cos^2\beta-1)\rangle=0.25$].

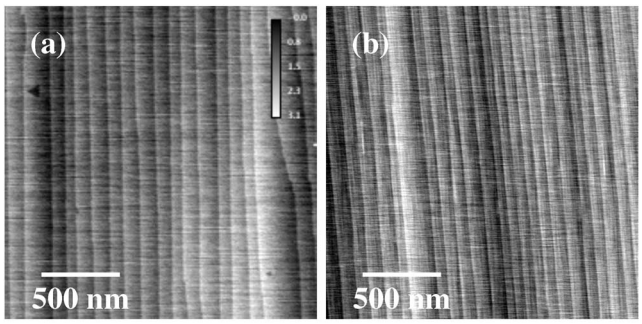

FIG. 5. AFM images of (a) a bare and (b) an amine-terminated Si(111) functionalized surfaces measured in air (Ref. 33). The step width of ~100 nm corresponds to a miscut of 0.2°.

III. REFLECTIVITY

AFM can be performed in solution with a lateral resolution of the surface morphology as small as several nanometers. It is a local technique, scanning only a small region of the surface. Reflectivity is a complementary, reciprocal-space technique that yields a model for the density profile $\langle\rho(z)\rangle_{xy}$ averaged over the surface. The use of x rays measures the electron density profile, neutrons can advantageously enhance the sensitivity or contrast through selective deuteration, and ellipsometry measures the optical index profile, all with atomic resolution in the $\hat{z}$ direction. For the study of DNA adsorption, we chose to perform x-ray rather than neutron reflectivity studies as the details of the physical chemistry are found to be affected[34] in D_2O. Nevertheless, we were inspired here by the neutron reflectivity technique to use contrast variation (see below) to improve the determination of the interface profile. Penetrating x-ray energies must be employed in the study of the liquid/solid interface.

X-ray reflectivity measurements do not necessarily require the use of a synchrotron radiation source. Indeed, the high flux available on a synchrotron beamline may prove to be quite damaging to organic systems and is a real concern in the study of biological samples. Nevertheless, the exposure times necessary when using a laboratory x-ray source may not be adapted to the system under study. We present here a comparison of results obtained both in the laboratory and at the synchrotron of x-ray reflectivity from the liquid/solid interface. (Measurements in vacuum to characterize similar monomolecular layers, covalently grafted on silicon substrates, have been reported previously in literature.[35]) Details of the x-ray reflectivity technique are given in the Appendix, in particular, concerning our measurement strategy.

A. Energy-dispersive reflectivity

Preliminary reflectivity experiments were first performed in the Department of Chemistry at the University of Bath, England by using an energy-dispersive reflectometer.[36,37] The continuous *bremsstrahlung* radiation from a tungsten

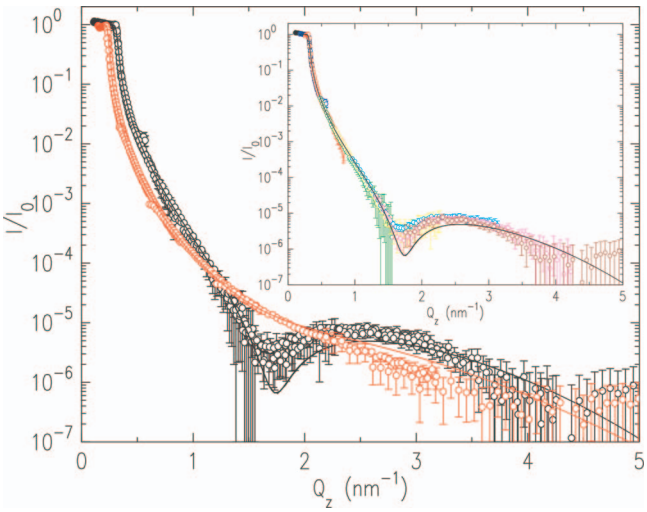

FIG. 6. (Color) A composite energy-dispersive reflectivity spectra of an amine-functionalized sample, as shown in Fig. 5, measured in air (black) and under buffer (red). The solid line shows the expected reflectivity according to the structural model fit to the data obtained at the ESRF, as will be presented below (see Fig. 9). The insert shows the data measured in air by fixed incidence angle: Black: 0.0405°, blue: 0.063°, red: 0.097°, green: 0.18°, yellow: 0.26°, cyan: 0.36°, magenta: 0.49°, and brown: 0.63°.

sealed-tube x-ray source, run at a stabilized high voltage of 55 kV and a regulated current of 25 mA (reduced to 15 mA when the samples were in air), is collimated by using tungsten slits and detected by using an energy-sensitive solid-state Ge detector. The high-energy end of the measured radiation spectra is limited by the applied high voltage. The low-energy falloff of the *bremsstrahlung* spectrum is attenuated additionally by absorption. The useful range of energies is ~15–55 keV for this instrument and a wavevector transfer range of ~3.6× is available for a given angle of incidence. The spectrum obtained upon reflection at a fixed angle of incidence is normalized to the transmitted, "white" spectrum acquired directly without reflection. A full reflectivity curve is acquired by using multiple angles of incidence, each with different slit openings to ensure a fixed incident beam "footprint" and a fixed angular resolution, $\Delta\theta/\theta=0.05$. An example of one such composite curve is shown in the insert to Fig. 6. The calibration of each segment in absolute reflectivity is complicated by the practice of not only opening the collimating slits with increasing angle of incidence but also by the opening of the slits in the direction out of the incidence plane with decreasing reflected intensity to improve the counting statistics. In addition, a constant background arising from the bulk diffuse scattering (that differs geometrically for each angle of incidence) must be subtracted from each acquisition. As will be shown below, this is a fundamental limitation in the confidence of the results obtained with this instrument.

The use of penetrating x-ray wavelengths allows the study of surfaces under an aqueous environment. The functionalized silicon sample is placed in the beam inside a small plastic box (polystyrene, dimensions of 40×18 mm^2 interior and 44×22 mm^2 exterior) and filled with a 1 mM sodium phosphate buffer solution ($NaH_2PO_4+Na_2HPO_4$, *p*H7.2). The resulting reflectivity spectra are shown in Fig. 6 in comparison with the spectra obtained in air. The two curves, of differing contrasts, can be analyzed together, as will be described in the following section.

The data obtained by using a laboratory x-ray tube source at Bath were quite satisfactory and served to justify the allocation of synchrotron beam time at the European Synchrotron Radiation Facility (ESRF). Indeed, the detection of the adsorption of double-stranded DNA is to be expected to require shorter data-acquisition times and even better counting statistics.

B. Fixed-energy reflectivity

A second strategy for measuring reflectivity uses a fixed wavelength, either the characteristic ray of a laboratory x-ray source or an undulator peak from a synchrotron radiation source. The latter was chosen as it presents the advantage of very high intensity and very low divergence, although at the risk of damaging the samples under study. This question will be addressed below.

Experiments were performed at the ESRF on beamline "ID10B."[38] The third harmonic of an undulator source is selected by a pair of diamond monochromator crystals (220). Lower-energy radiation is filtered and the beam is focused in the horizontal plane by a pair of mirrors and in the vertical plane by a third mirror. The highest energy available on this beamline due to geometrical constraints is 22.2 keV ($\lambda=0.0559$ nm). The minimum beam size that can be focused incident on the sample is ~50 μm in the vertical incidence-plane. At the critical angle of incidence for a water/silicon interface, 1.06 mrad at this energy, the beam footprint is, thus, ~47 mm. The vertical beam size can be further reduced to about half this height by using limiting slits before the sample (~0.02×1 mm^2); however, the very high spatial coherence of the undulator beam yields diffraction effects with such a small vertical slit.

The sample was placed in a polytetrafluoroethylene (PTFE) cell with 50 μm semicrystalline flourinated ethylene propylene copolymer (FEP) windows to allow aggressive chemical cleaning (piranha solution) and to prevent any DNA adsorption on the cell walls. The thin copolymer windows were held in place by two aluminum-alloy flasks (see Fig. 7). The x-ray transmission of the cells filled with buffer solution was measured to be $(15\pm2)\%$ for an ~30 mm path length. The functionalized silicon substrates were cut to 30 $\times24$ mm^2 from a 4 in. wafer; the thickness (0.5 mm) was, in fact, insufficient to assure the strict planarity of the substrate, as will be observed below.

The greater transmission through the 3 cm sample cell filled with water at higher x-ray energies is accompanied by a decreasing critical angle for total external reflection. The geometrical beam footprint increases linearly with decreasing incidence angle, therefore, linearly with increasing x-ray beam energy (for a fixed value of the wavevector transfer). Therefore, for a fixed sample size, this would require a corresponding reduction in vertical beam dimension, thus a (linear) reduction in incident x-ray beam intensity that ultimately limits the advantage of using higher-energy x rays.

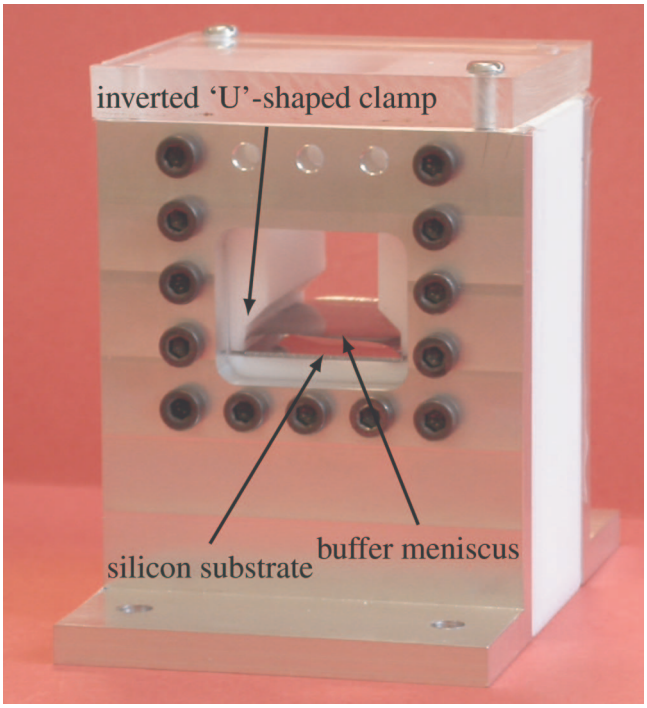

FIG. 7. (Color) PTFE sample cell. The horizontal silicon wafer is covered by the buffer solution whose meniscus against the thin copolymer windows can be seen in the photograph.

The transmitted (with the solid surface lowered out of the beam path) as well as the reflected beams were detected by using a NaI(Tl) scintillator and photomultiplier. The incident beam intensity was $\sim 10^{10}$ photons/s (or 40 μW) which varied according to the synchrotron electron-beam current. A wheel holding an increasing number of pure copper 46 μm foil filters that were placed *before* the sample was used to variably attenuate the incident beam. The detector arm angular resolution was limited by slits (0.2×1 mm^2) located before the detector, 640 mm from the sample (a second pair of slits located on the detector arm 190 mm from the sample was kept relatively open at 5×5 mm^2). The detection angular resolution was, thus, $\Delta\theta_{out}=0.0179°$ in the vertical plane. The incident beam divergence $\Delta\theta_{in}$ was somewhat smaller than that of the undulator source ($\sim 0.001°$).

C. Stability of functionalized Si surfaces under irradiation

The very high intensity of the synchrotron radiation beam can rapidly degrade the thin organic functionalization layers of samples to be studied, both from photoelectrons ejected from the silicon substrate upon absorption of the penetrating x-ray beam and through ionization of the buffer or air (principally through the production of ozone). In order to assess and control this undesirable effect, we first studied under the synchrotron beam a sample that was covered by a dense, organic monomolecular layer with a terminating acid group, an early step in the chemical process of functionalization.[39] The results are shown in Fig. 8 for the sample measured at two contrasts: Both in air and under 1 mM sodium phosphate buffer solution.

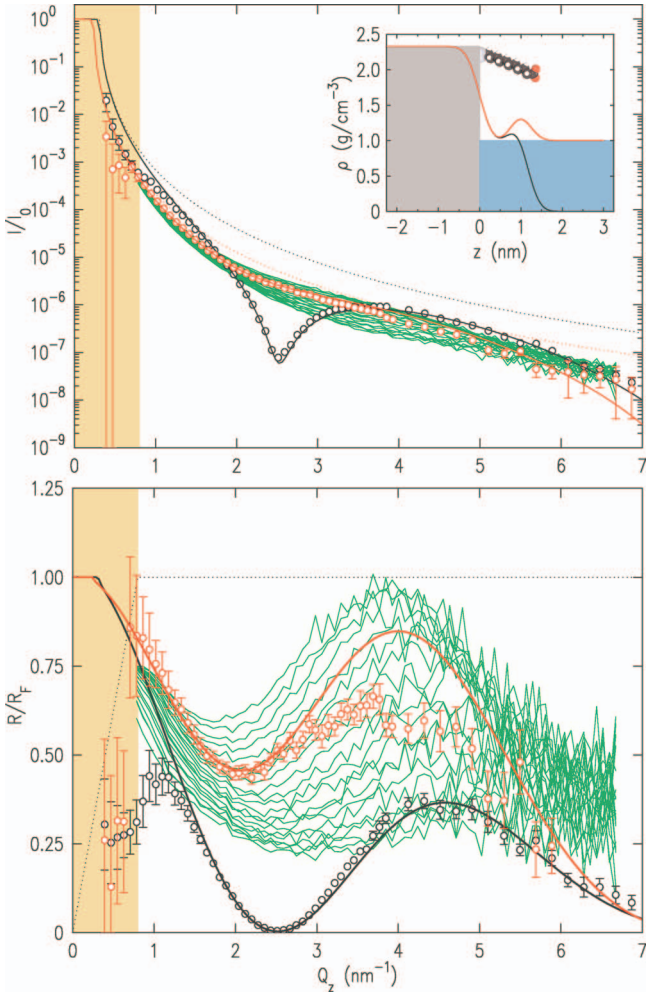

FIG. 8. (Color) Acid-terminated functionalized silicon sample. Top: Reflectivity and bottom: Normalized to the Fresnel step reflectivity (Black: In air and red: Under buffer solution). The insert shows the real-space density profiles as continuous lines that describe the data shown in reciprocal space. The molecular model in real space (see Fig. 3) is drawn schematically for illustration. The series of continual (green) traces present a succession of fairly rapid (about 9 min), reflectivity curves measured under buffer solution and showing sample degradation under irradiation.

A rocking curve was recorded for each angle of incidence, and it was observed that the sample was, in fact, slightly curved, leading to a widening of the rocking curves (see Appendix, Fig. 19) by about a factor of 2 (this corresponds to a radius of curvature of the silicon surface of the order of 50 m). Indeed, it was observed that this curvature could be aggravated by a very slight pressure on the inverted U-shaped clamp used to hold the substrate in place inside the sample cell (see Fig. 7). The observed widening of the rocking curves was compensated in the calculation of the reflectivity through a normalization to the areas under the peak by using an analytic two-slit function [see Appendix, equation (A5)]. Data at low values of the wavevector transfer, in particular, the "plateau" of total external reflection, were not recorded, for it was not possible to reduce the beam size sufficiently for such small angles of incidence.

In order to determine the possible degradation of the organic layer under irradiation, a series of fairly rapid direct reflectivity curves (scans of $\theta_{in}=\theta_{out}$, often called "θ:2θ")

TABLE I. Parameters of the models used to describe the data. IR indicates the results of surface infrared spectroscopy quantification (see, for example, Ref. 40). The numerical surface densities are found to be less than half that of Si—H binding sites on the Si(111) surface (7.8×10^{14} Si/cm^2). The area/molecule for the grafted monomolecular layer is the inverse of the numeric surface density and is to be compared to that of a dense alkyl chain: 0.214 nm^2 for liquid paraffins (Ref. 69), 0.205 ± 0.01 nm^2 for monolayers of fatty acids (Ref. 70) and 0.185 nm^2 for crystalline *n*-hydrocarbons (Ref. 71).

	Thickness (nm)	Roughness (nm)	Surface density (10^{-7} g cm^{-2})	Surface density (10^{14} cm^{-2})	Area/molecule (nm^2)
Fig. 8:					
acid	1.085 ± 0.025	0.254 ± 0.011	1.26 ± 0.06	3.6 ± 0.2	0.28 ± 0.02
IR				3.0 ± 0.3	0.33 ± 0.03
Fig. 9:					
amine 1	1.504 ± 0.114	0.354 ± 0.004	1.54 ± 0.15	3.4 ± 0.3	0.29 ± 0.03
IR				3.1 ± 0.3	0.32 ± 0.03
+dsDNA	1.5	0.354	1.888 ± 0.009		
→excess			0.35 ± 0.16		
Fig. 13:					
amine 2	1.62 ± 0.16	0.31 ± 0.02	1.82 ± 0.22	4.0 ± 0.5	0.25 ± 0.03

was successively recorded for the sample under buffer solution (green traces in Fig. 8, starting from the upper trace). Because of the curvature of the substrate and the widening of the specularly reflected beam, the data normalized to the maximum I_0 of the transmitted beam had to be corrected according to the same linear function as found for the widening of the recorded rocking curves. A constant background of diffuse scattering is subtracted, as determined by a fit at large angles of incidence ($Q_z>6$ nm^{-1}). The contrast of the interference fringe is observed to sequentially diminish under irradiation. The reduction in reflected x-ray intensity observed here is characteristic of an effective reduction in area of intact surface monomolecular layer under the illuminated beam.

Through an attenuation of the incident beam intensity (by a factor of 60) and an optimization of the data-acquisition times and spacings, as well as the adoption of a procedure of laterally displacing the sample by 1 mm in the direction perpendicular to the incident plane, highly reproducible results were obtained, superimposing the upper green trace of Fig. 8 (data not shown).

D. Analysis of the reflectivity curves

In the bottom of Fig. 8, the same data as shown in the top of the figure are represented, divided by the calculated Fresnel reflectivities of an ideal, step air/silicon and water/silicon interfaces, neutralizing the overall Q_z^{-4} dependence. Also shown as (red and black) solid lines are a fit to a simple model for the density profiles. The real-space model is drawn as an insert to Fig. 8; the two profiles (in air and under buffer) only differ by the index of the semi-infinite media. The parameters obtained for the data are summarized in Table I.

X-ray reflectivity measures a root-mean-squared roughness that is a weighted average of the height-height correlation function over length scales ranging from the atomic dimensions up to the surface in-plane correlation length as given by the resolution of the instrument. This roughness is found to be 0.25 ± 0.01 nm, larger than the ideal, expected value of ~0.15 nm [see the discussion following Eq. (2)]. The nominal thickness of the acid-terminated organic layer is found to be 1.09 ± 0.03 nm. The surface density of molecules determined by x-ray reflectivity is in good agreement with the value obtained by surface infrared spectroscopy[40] on an equivalent acid-terminated surface.[33] The inverse of this quantity is the area occupied on average by each molecule (0.28 ± 0.02 nm^2/molecule, as determined by x-ray reflectivity). The cylindrical average volume occupied by each grafted molecule is represented in Fig. 3(a).

The model divides the real-space profile into two *fictitious* layers of constant density, associated with up to two fitting parameters per layer: The density ρ and the thickness. In fact, the free fitting parameters are quite correlated, especially when the thickness is of the same order of magnitude as the overall roughness (a fifth fitting parameter), which is, indeed, the case for the present sample. The method employed here of simultaneously fitting measurements obtained with two different contrasts, as is commonly the practice for neutron scattering, robustly converges to the displayed density profiles with reasonably low quantitative uncertainties. Notice the absence of any oxide layer.

We would like to insist here on the interpretation of the determined density profiles, as shown in the inserts of Fig. 8. Whereas the profiles $\rho(z)$ can be constructed by using "layers" of constant density, such a construction is overdetermined, in particular, when the "thickness" of each layer is of the same order of magnitude as the roughness, and this fact is reflected in the coupling of the model parameters, as stated in the previous paragraph. Nevertheless, the overall thickness of the grafted layer, its integral mass-density excess, and the general form of the profile are well determined by the models, and only these parameters will be considered in the interpretation of the results presented here. A reasonable conceptual illustration can be seen in Fig. 3 where the transparent cylinders centered on the silicon atom anchors

for the grafted organic molecules show the molecular volumes as determined by x-ray reflectivity. We note that the fully extended molecular models extend outside and above these cylindrical volumes, but this is no longer the case for a model that introduces some molecular disorder[41,42] (both static and dynamic).

E. Structure of the amine-functionalized surface

The amine-terminated surface shown in Fig. 5 was studied by x-ray reflectivity as described above for the acid-terminated samples, but under conditions where the degradation by the synchrotron beam was minimized. Mostly, direct reflectivity curves were recorded, as shown in Fig. 9; only the red-solid filled and several black-solid filled data points (hardly visible in the already crowded graphical representation) correspond to the result of rocking curves. Here, in contrast to the measurements on the acid-functionalized surface shown in Fig. 8, data at small values of the wavevector transfer are shown; the maximum reflectivities recorded under conditions of total external reflection were only 32% in air and 36% under buffer solution when normalized to the real direct-beam intensity. It can be seen by the linear rise in the data for $Q_z < 1\ \mathrm{nm}^{-1}$ in the Fresnel-normalized data shown in the bottom of Fig. 9 that this is a simple effect of the incident beam footprint overhang. One should note that the very common practice of normalizing the reflectivity curve to the plateau of total external reflection would here lead to a systematic error of about a factor of 3!

The data drawn in black (in air) and red (under buffer solution) are well described by a simple model for the density profiles (shown in the insert to Fig. 9), as was the case for the acid-terminated sample presented above. The root-mean-squared roughness is (0.354 ± 0.004) nm and the organic layer thickness is (1.5 ± 0.1) nm, both somewhat larger than those found for the acid-terminated functionalized surface, as expected. Indeed, the diamine terminal group is believed to lie somewhat disorganized, as the amine (NH_3^+) functionalization of the monomolecular layer is incomplete with some of the grafted molecules retaining their terminal acid (COOH) or ester (COO^-) groups.[33] In addition, this leaves some possibility of bridging between head groups.

The surface density of molecules is again in good agreement with the value as determined by surface infrared spectroscopy,[33,40] and the coverage of available Si—H binding sites is estimated to be $(44 \pm 4)\%$ (see Table I). We note also that this surface density corresponds to an area per molecule of $(0.29 \pm 0.03)\ \mathrm{nm}^2$ [see Fig. 3(b)], which is only about 40% greater than that of a very dense-packed alkyl chain. The organic monolayer, covalently bonded to the silicon crystal lattice, has a surface density corresponding to a tilted condensed phase.[43] For a dense-alkyl chain at the expected tilt angle of $35°16'$, the area per molecule projected on the surface plane would be $0.26\ \mathrm{nm}^2$, only slightly smaller than the x-ray reflectivity value, and within our experimental error.

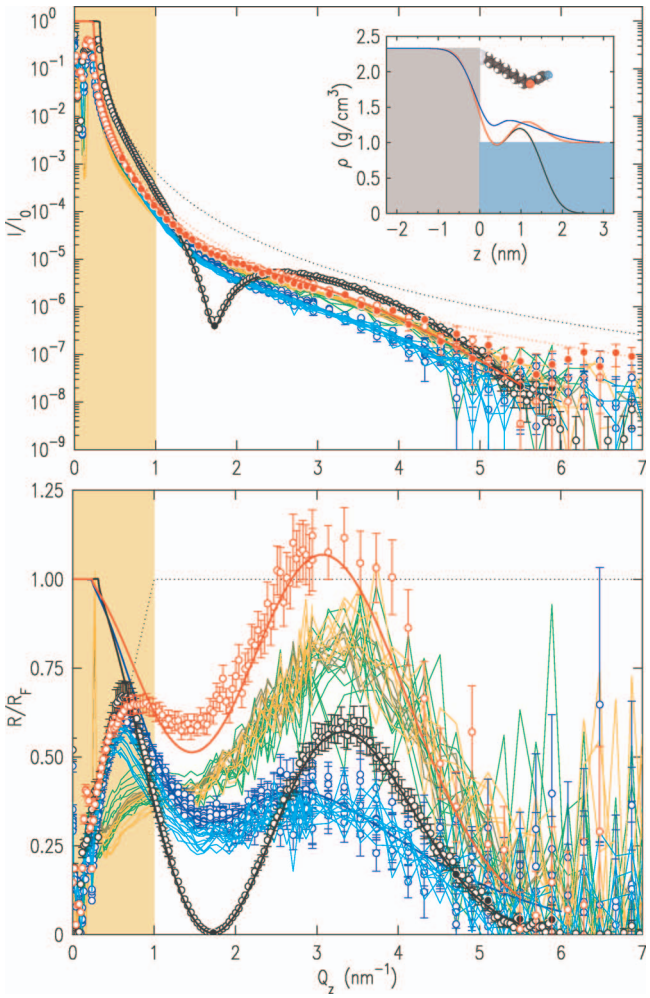

FIG. 9. (Color) Amine-terminated functionalized silicon sample. Top: Reflectivity and bottom: Normalized to the Fresnel step reflectivity (Black: In air, red: Under buffer solution, and blue: Under buffer after DNA adsorption). The (red- and black-)filled symbols are the results of rocking curves recorded for each angle of incidence and the open symbols are direct reflectivity scans (a few black-filled symbols can be seen to overlie the black open symbols). The insert shows the real-space density profiles as continuous lines that describe the data shown in reciprocal space. The molecular model in real space (see Fig. 3) is drawn schematically for illustration. The continual (green, olive, and orange) traces are an intermediate state following the addition of increasing concentrations of DNA to the buffer solution: $1 \times C^\star$, $3 \times C^\star$, and $10 \times C^\star$, respectively. The (blue) data (lowest lying curves) were recorded at this last concentration 6 h after the first introduction of DNA to the cell. The (blue) solid lines show a model density profile (insert) describing this data. The (cyan) traces show the reproducibility of this profile following the addition of a much greater quantity ($5\times$) of DNA ($\rightarrow 60 \times C^\star$).

F. DNA adsorption on the amine-functionalized surface

DNA adsorption is expected at a positively charged surface, such as the amine-functionalized molecular monolayer under the present buffer conditions (1 mM sodium phosphate buffer, *p*H 7.2).

1. Double-stranded DNA

The mass density of double-stranded DNA is very close to that of water. For example, at low salt concentrations, similar to our experimental conditions, the density is reported to be $0.998\ \mathrm{g/cm}^3$ (at 10 mM NaCl).[44] Therefore, on

TABLE II. 294 bp double-stranded DNA.

5′-ACTTTGCGACCTTTCGCCATCAACTAACGATTCTGTCAAAAACTGACGCGTTGGA
TGAGGAGAAGTGGCTTAATATGCTTGGCACGTTCGTCAAGGACTGGTTTA
GATATGAGTCACATTTTGTTCATGGTAGAGATTCTCTTGTTGACATTTTAAAAGAGCGTG
GATTACTATCTGAGTCCGATGCTGTTCAACCACTAATAGGTAAGAAATCATGAGTCAAGT
TACTGAACAATCCGTACGTTTCCAGACCGCTTTGGCCTCTATTAAGCTCATTCAGGCTTC
TGCCGTTTT-3′

average, there will be very little electron density contrast with water and it is not to be expected to be able to easily detect the adsorption of a *disordered* layer of DNA by x-ray reflectivity. Over 100 μg of monodisperse, double-stranded DNA molecules was prepared by polymerase chain reaction (PCR) amplification from a 294 base-pair (bp) sequence of the 5386 bp ϕX174 DNA (locations 175–470) (see Table II). Supercoiled, double-stranded ϕX174 (circular replicative form RFI) was used as a PCR template. The amplified DNA was purified by using a Sigma-Aldrich GenElute™ PCR cleanup kit and the quality of the final product was analyzed by using polyacrylamide gel electrophoresis.

The length of the 294 bp double-stranded DNA fragment, $294\times0.34=100$ nm, is comparable to one persistence length when adsorbed on a surface at the present low-salt concentration,[45–47] and the molecule can be viewed as a semirigid cylinder of diameter 2 nm (see Fig. 10). This diameter is equal to about two and a half times the spacing of two adjacent organic molecules, covalently bonded to the single-crystal silicon substrate and slightly greater than the thickness of the organic layer. Taking the cylinder to be adsorbed lying flat on the surface, its projected surface area would then be $2\ \text{nm}\times100\ \text{nm}=200\ \text{nm}^2$. If the surface were to be densely packed by a sort-of two-dimensional (2D) nematic phase, thus completely covered by adsorbed cylinders of double-stranded DNA, the required quantity for total coverage of the $3\times2.4\ \text{cm}^2$ surface is $(294\ \text{bp}\cdot660\ \text{g mole}^{-1}\ \text{bp}^{-1}/N_A)\cdot(7.2\times10^{14}\ \text{nm}^2/200\ \text{nm}^2)=1.16\ \mu\text{g}$. As the volume of buffer contained in the sample cell is 1.7 ml, the reference concentration to be used in the following is $C^\star\equiv1.16\ \mu\text{g}/1.7\ \text{cm}^3=0.68\ \mu\text{g}/\text{cm}^3$.

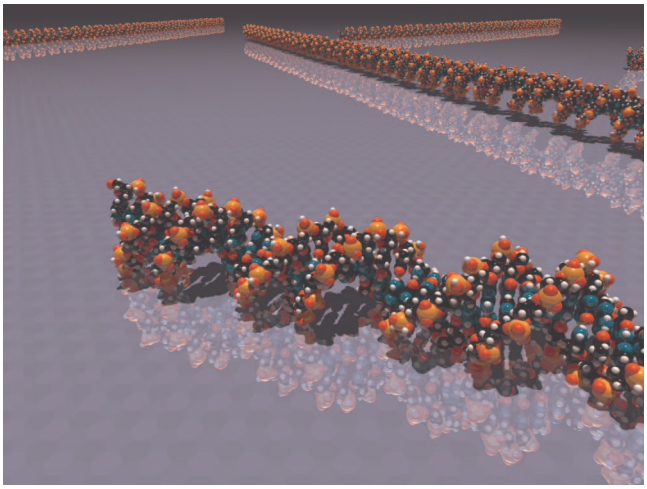

FIG. 10. (Color) Molecular model of 294 bp double-stranded DNA fragments adsorbed on a solid surface.

After the characterization of the amine-functionalized sample both in air and under buffer, as presented above, we proceeded to mix a small quantity of DNA (equivalent to "$1\times C^\star$," as calculated above) in the buffer solution, followed by measurements of the reflectivity curve. The procedure adopted was to gently remove as much buffer as possible, assuring that the surface remain to be entirely wet. The removed buffer was mixed with the DNA solution and then redeposited over the wet silicon surface. This assured a uniform distribution of DNA. The thickness of the remaining wetting layer can be estimated to be on the order of 100–200 μm. The measured reflectivity curves reproduced one another to a very good accuracy (light-green traces as drawn on Fig. 9, each individual trace taking about 9 min to acquire). However, as can be more clearly seen in the Fresnel-normalized reflectivity (bottom of Fig. 9), these curves lie slightly lower than those measured before the addition of DNA to the buffer solution. After 2 h (11 repeats of the reflectivity curve), more DNA ("$3\times C^\star$") was added and the sample was displaced laterally (with realignment) to expose a fresh patch of substrate (orange traces in Fig. 9).

The measurement was repeated for 1 h (five olive-green traces as drawn on Fig. 9) with no change from the previous curves in the measured reflectivity. More DNA was added ("$10\times C^\star$") and the sample again displaced, with still no change in the reflectivity curves at large wavevectors (orange traces). After almost 3 h following the third introduction of increasing quantity of DNA (6 h after the initial introduction of DNA), a significant change in the reflectivity curve was recorded (blue traces in Fig. 9). This new reflectivity curve remained to be stable, unchanging over about 1.5 h, as measured over two different patches of the sample surface. Finally, additional DNA was added ("$60\times C^\star$") and the sample again displaced. The recorded reflectivity curve remained to be reproducible (cyan traces in Fig. 9). Over 12 h elapsed since the initial introduction of DNA in the sample cell.

Assuming that the adsorption of DNA is diffusion controlled, the quantity of material adsorbed would be expected to vary as the square root of the time, as given by[48–50] $\Gamma=2C\sqrt{Dt/\pi}$, where C is the (uniform) bulk concentration and D is the diffusion coefficient. Taking a diffusion coefficient for the 294 bp double-stranded DNA estimated to be $D\approx3\times10^{-7}\ \text{cm}^2\ \text{s}^{-1}$, the time necessary for a DNA molecule to diffuse the distance from the air/water to the water/Si interface ($h=1.7\ \text{cm}^3/7.2\ \text{cm}^2=0.24$ cm) would be[51] $\langle h^2\rangle/6D=(0.24\ \text{cm})^2/(3\times10^{-7}\ \text{cm}^2\ \text{s}^{-1}\cdot6)=3.2\times10^4$ s $=9$ h. Note that this time is of the same order as the 6 h that

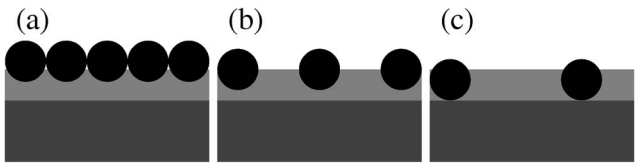

FIG. 11. Embedding of the adsorbed DNA molecules. Black circles: DNA, light gray: Surface monomolecular layer, and dark gray: Silicon monocrystalline substrate. (a) 100% coverage (0.4 nm), (b) 50% coverage (1 nm), and (c) 31% coverage (1.5 nm).

was necessary for each reflectivity measurement. In the present experiments, we were unable to capture the kinetics of the adsorption and, thus, it would be hazardous to speculate further on the adsorption process.

An analysis of the reflectivity curves observed with adsorption of DNA on the amine-terminated monolayer leads to the model for the real-space density profiles drawn in the insert to Fig. 9 (blue curve) using the parameters listed in Table I: The overall layer thickness is not modified, yet the region of increased density of the amine-head groups of the functionalized layer is enlarged, with additional (electron) density filling in the region previously occupied by the alkyl chains. The increased integrated surface mass density can be quantified, yielding an increase in mass density of $(0.35 \pm 0.16) \times 10^{-7}$ g/cm^2. This measured quantity, multiplied by the theoretical projected area per bp of an adsorbed DNA molecule $(0.68 \times 10^{-14}$ cm$^2)$ and by N_A is 143 ± 65 g/mole (22% of the molar mass of a bp of DNA).

If the surface were to be totally covered by a dense layer of DNA (which is less likely due to the repulsion between DNA helices), the increase in surface-layer mass density would imply that one-fourth of the DNA molecule would enter into the monolayer; the opposite extreme of full embedding of the DNA molecule all the way down to the bare silicon surface would imply that the saturated surface coverage is only about 31% but this situation seems to be impossible. The reality must be a surface coverage lying in the range of 31%–100% with a partial integration into the dense but soft surface layer, most likely limited to the region of the functionalized head groups. This is illustrated schematically in Fig. 11. Attempts to place the additional, significant electron density *above* the organic monolayer could not describe the measured data (remember that the density contrast with the displaced water is very low) nor did we succeed to describe the data by using a model including an oxidation of the silicon surface. We conclude that the adsorption of DNA molecules distorts the grafted monolayer. The "roughness" of the amine-head region of the density profile increases, the (electron) density of the chain region increases, but the average thickness of the monolayer is unmodified.

Unlike what was described in the previous paragraph, the change in the measured reflectivity curves observed for the first curves following the introduction of double-stranded DNA in the solution is difficult to describe quantitatively through a unique density profile model. Qualitatively, this may be the effect due to the deposition of patches of DNA aggregates, reducing the effective area of the monomolecular layer over a large, lateral length scale. This surface organization is, however, transitory with the subsequent reflectivity curves returning to an expected behavior at lower values of the wavevector transfer.

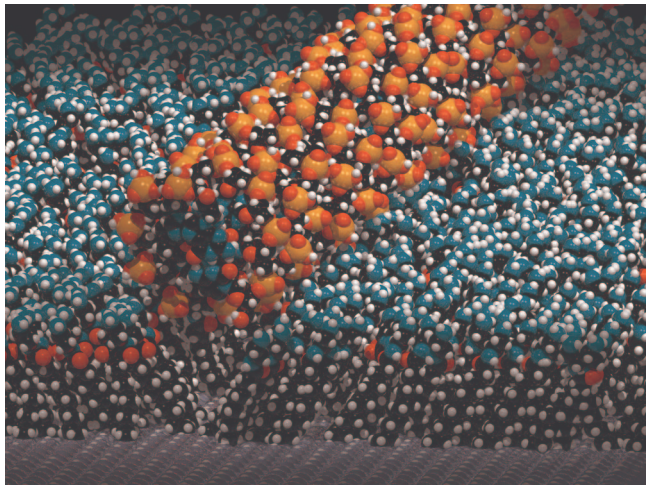

FIG. 12. (Color) Molecular model of an isolated double-stranded DNA molecule adsorbed on the positively charged, amine-functionalized surface.

We questioned that the observed change in the reflectivity curves observed after a longer adsorption time and for higher bulk concentrations, indeed, corresponds to the adsorption of double-stranded DNA. Several tests were performed:

- The addition of salt might lead to a desorption of the DNA. NaCl solutions of 10, 50, 100, 300, and 500 mM were added to the sample cell and reflectivity curves were measured. The adsorption of DNA appeared to be irreversible and the reflectivity curves remained to be unchanged (data not shown).
- Many different zones of the sample were measured, with very reproducible results.
- The previously studied acid-terminated surface was re-examined after several *days* under buffer solution (ageing of the monolayer) and the reflectivity curves were reproducible.

The adsorption of double-stranded DNA on a positively charged functionalized, atomically flat silicon surface is observed, not through an increase in the thickness of the surface layer or added electron density above the organic monolayer as might be expected but rather through a deformation of the (soft) surface functionalized layer and the incorporation of additional electron density in the layer. A naïve model of the adsorption is drawn in fig. 12. An electrostatic attraction between the positively charged amine groups of the monolayer (with a surface charge density of $\leq 3.1^+/\text{nm}^2$ which is an upper limit, assuming that the amine groups are fully charged and a complete functionalization of the monomolecular layer) and the negatively charged phosphate groups of the nucleic acid (with a projected charge density of $2^-/0.68\ \text{nm}^2 = 2.9^-/\text{nm}^2$) would "pull" the DNA molecule into the monolayer in order to maximize contact with the negative charges distributed helically around the perimeter of the rigid cylinder, displacing the mobile counterions. We

have no solid evidence for this model other than the coherence with the measured reflectivity curves density profiles. The adsorption taking place under low ionic strength (1 mM sodium phosphate buffer, *p*H 7.2) is found to be irreversible, even under conditions of much higher added salt concentrations (up to 500 mM NaCl). This suggests that a partial dehydration of the DNA molecule is also involved in the adsorption on the organic monolayer and the interaction may, indeed, be even more complicated[52,53] with the further possibility of hydrogen bonding with the residual acid groups. Further information regarding the in-plane organization of the adsorbed DNA might be obtainable through grazing-incidence diffuse scattering[54] analysis and grazing-incidence surface diffraction[55] measurements, but these experiments would require considerable time and effort to optimize.

2. Reproducibility of the amine-functionalized surface

A second amine-terminated monolayer grafted on silicon substrate was studied, according to the same procedure as for the first. The results obtained for the characterization of the grafted surface layer yield a very similar density profile as for the previous sample and demonstrates the reproducibility of the surface chemistry as well as the reflectivity measurements. However, unlike for the first sample studied, no rocking curves were recorded for this second sample and there is, therefore, an ambiguity as to the actual curvature of this silicon substrate.

The results obtained to characterize the second amine-terminated monolayer grafted on the monocrystalline silicon substrate are shown in Fig. 13. In the data presented here, we use the same curvature correction for this second sample as measured for the first, in the absence of any better estimation, as described above. This leads to some incertitude as can be seen by the poor overlap of the curves at very grazing angles of incidence (as best illustrated in the Fresnel-normalized representation, bottom of Fig. 13) and by the somewhat lower quality of the fit of the simple model density profiles to the measured reflectivity curves. In particular, the simultaneous adjustment of the data measured at the two different contrasts (both in air and under buffer), which was so successful for the previous measurements, here leads to a compromise, and the description of the data at high values of the wavevector transfer is only qualitatively satisfactory. We have less confidence in these measurements than for the previous sample, therefore, the addition of further, short length-scale details in the model density profile cannot be justified.

3. Single-stranded DNA

The sample was then exposed to a buffer solution containing single-stranded DNA. A single-stranded oligonucleotide, 146 bases long (44 669.25 g/mole, see Table III), was prepared by chemical synthesis (Eurogentec SA). Single-stranded DNA differs radically from the double-stranded helix in its properties: It is a highly flexible polymer (persistence length on the order of less than 1 nm), with its bases exposed to the solvent. In this case, it is difficult to present a

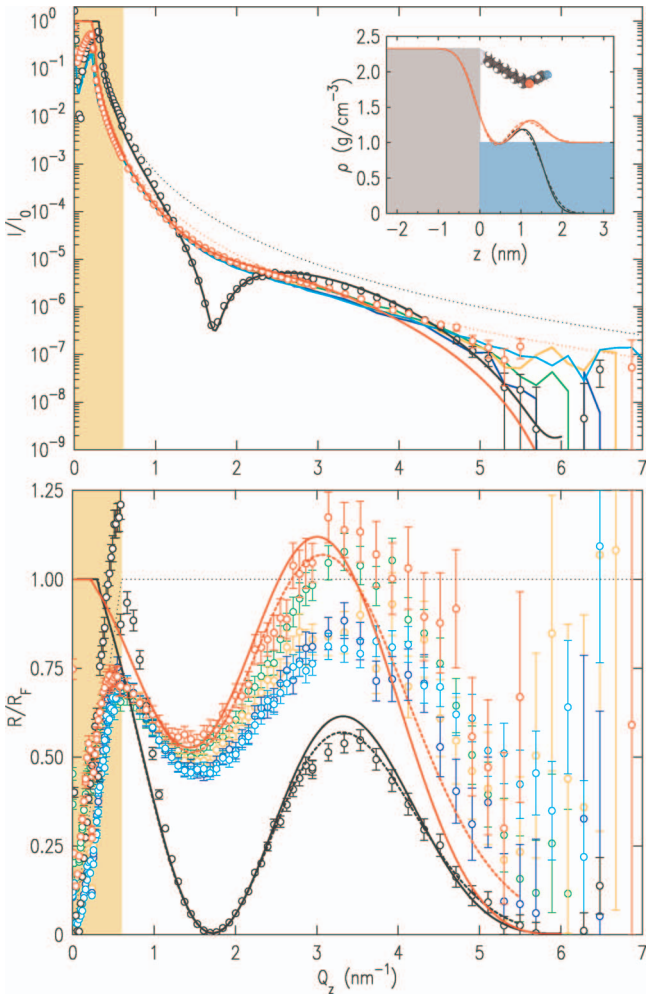

FIG. 13. (Color) Single-stranded DNA on an amine-terminated functionalized silicon surface. Top: Reflectivity and bottom: Normalized to the Fresnel step reflectivity. The open symbols are direct reflectivity scans. The insert shows the real-space density profiles used to model the data. The solid lines are the result of a fit to the data and the dashed lines are the profiles and corresponding reflectivities from Fig. 9. (Black: In air and red: Under buffer solution). The lighter symbols (green, orange, cyan, and blue) parallel those of Fig. 9.

simple model of a rigid cylinder that can be adsorbed on a functionalized surface, rather one should consider a 2D radius of gyration of the flexible polymer with excluded volume. Nevertheless, to a first approximation and with the aim of later studying the hybridization with the complementary single strand, we used a reference concentration considering naïvely that the adsorbed single-stranded DNA occupies half the area of the equivalent double-stranded DNA (i.e., that the base stacking is conserved.); the concentration $C^{\star}$, taken to be 1.08 μg/1.7 cm^3=0.63 μg/cm^3 is, thus, the same as the previous one (0.68 μg/cm^3).

Measurements were repeated as for the first amine-terminated sample after addition of increasing quantities of DNA. The results are plotted in Fig. 13 (using the same color coding as in Fig. 9). Almost no change in the reflectivity curves is observed, certainly much less than the changes observed for the previously presented radiation damage on the acid-terminated sample and the double-stranded DNA adsorption on the positively charged amine-terminated sample.

TABLE III. 146 base single-stranded DNA.

5′-AAGCTTGTATGATCACTCGTCGATCCACATCAGTATGATCACTCGTCGATCCATATACAT CAGTATGATCACTCGTCGATCCATATACATCAGTATGATCACTCGTCGATCCATATACAT ATGATCACTCGTCGATCGAATTCCAT-3′

However, when plotted on a linear scale after normalization by the Fresnel step reflectivity (bottom of Fig. 13), a small yet systematic decrease in the fringe intensity is evidenced, at the limit of our measurement precision (the cyan and blue curves at higher concentration of DNA being lower than the orange and green curves at lower concentration as well as the red curve obtained under buffer before the addition of the single-stranded DNA). Note that each of these reflectivity curves was measured over freshly exposed portions of the sample surface and is not to be compared to the continual decrease in fringe contrast with irradiation as observed for the very first, acid-terminated sample studied before reduction of the x-ray beam intensity.

Single-stranded DNA may be adsorbed on the positively charged aminated surface but does not lead to a distortion of the organic monolayer and is not unambiguously detected. Some subtle structural differences may be measurable, but we cannot have sufficient confidence in the present data to push the analysis further.

IV. CONCLUSIONS

The DNA adsorption in a low ionic strength buffer was characterized on crystalline silicon by x-ray reflectivity. The functionalized single-crystal silicon surfaces were chemically controlled: Oxide-free, densely and homogeneously covered by organic molecules. The molecular monolayer was terminated by positively charged amine groups, yielding a strong electrostatic interaction with the negatively charged DNA.

It was found that the adsorption of double-stranded DNA leads to a distortion of the organic monolayer. The double-stranded DNA penetrates into the organic monolayer and, as this adsorption is irreversible by adding salt in the solution, we conclude that DNA chains are partially dehydrated. The additional mass density of the adsorbed DNA that is deduced in the surface layer corresponds to about one quarter of that expected for a densely packed adsorbed layer of DNA molecules lying flat on the surface. The DNA partially penetrates the soft surface layer. We did not observe such an important effect by adsorbing single-stranded DNA.

In the present work, we have shown that a solid surface, functionalized by a near-perfect, thin organic monolayer, must not be viewed as an inert, solid support. The densely packed organic monolayer is soft and deformable, as seen through the adsorption of double-stranded DNA molecules. This understanding should be of great importance in the development of DNA biochip and lab-on-a-chip technologies.

ACKNOWLEDGMENTS

The synchrotron x-ray experiments were performed at the ID10B beamline of the European Synchrotron Radiation Facility, Grenoble, France with the skillful assistance of Alexei Vorobiev and Oleg Konovalov. The DNA samples were prepared with the assistance of Arach Goldar (Service de Biologie Intégrative et de Génétique Moléculaire, CEA/Saclay), whom we also thank for many useful discussions. We also thank Philippe Allongue for his advice in the preparation of the substrates and Rabah Boukherroub of the CNRS for financial support for the Ph.D. thesis of C.D. The molecular models presented here were rendered by using the POV-ray (http://www.povray.org/) ray tracing tool. We are grateful to François Ozanam (LPMC, Ecole Polytechnique) and to Jean-Louis Sikorav (Service de Physique Théorique, CEA/Saclay) for their conscientious reading of the manuscript and to an anonymous referee for his or her suggestions.

APPENDIX: X-RAY REFLECTIVITY

The reflectivity technique is now well established. Nevertheless, many subtleties involved in its application are still not commonly appreciated and we present here a detailed description of the technique as it is employed in the present study.

1. X-ray reflectivity

The optical index for x rays depends on the wavelength, is inferior to unity for all matter, and is complex,

$$n(\lambda) = 1 - \delta(\lambda) + i\beta(\lambda), \tag{A1}$$

with

$$\delta(\lambda) = \rho\lambda^2 \frac{N_A}{2\pi A}[Z + \Delta f'(\lambda)]r_0, \quad \beta(\lambda) = \frac{\mu(\lambda)\lambda}{4\pi}, \tag{A2}$$

where ρ is the mass density, $N_A = 6.023 \times 10^{23}$ is Avogadro's number, λ is the x-ray wavelength, A is the atomic weight, Z is the atomic number, $\Delta f'(\lambda)$ is the (zero angle) dispersion correction to the atomic scattering factors due to core-electron screening[56], $r_0 = 2.818 \times 10^{-13}$ cm is the classical electron radius for Thompson scattering, and $\mu(\lambda)$ is the wavelength-dependent absorption coefficient (inverse of the absorption length). For 22.2 keV x rays used in the present synchrotron measurements, the e^{-1} absorption length in water is 1.44 cm. The quantity $\delta(\lambda)$ is directly proportional to the mass density and to the square of the wavelength, as the ratio Z/A is a constant and equal to $1/2$ to a good approximation for all chemical compositions under study. Note that the formalism for neutron reflectivity is the same, however, substituting nuclear scattering lengths b, which differ for each isotope, for the quantity Zr_0 in Eq. (A2). The neutron scattering-length-density profile is not trivially proportional to the mass-density profile, and this may be advantageous to enhancing contrast.

Total external reflection of grazing-incidence x rays occurs up to a critical angle $\theta_c \approx \sqrt{2\Delta n}$, where $\Delta n = \delta_- - \delta_+$ is

the difference in x-ray optical indices between the two semi-infinite media. Thus, the critical angle, $\theta_c \approx \lambda\sqrt{\Delta\rho N_A r_0/2\pi}$, is proportional to the wavelength and is calculated to be 0.0802° (1.40 mrad) for the air/Si interface and 0.0607° (1.06 mrad) for the H_2O/Si interface at $\lambda = 0.055\,86$ nm, $hc/\lambda = 22.2$ keV; the critical wavevector transfer, $Q_c = (4\pi/\lambda)\theta_c = 2\sqrt{2\pi\Delta\rho N_A r_0}$, is a constant, independent of the x-ray wavelength (0.315 and 0.238 nm^{-1}, respectively, for the air/silicon and water/silicon interfaces).

At larger angles of grazing incidence, the reflectivity $I(\theta)/I_0$ decreases rapidly with angle of incidence, as given by the Fresnel law which can be approximated beyond about twice the critical angle of total reflection by

$$R_F(\theta) \approx (\theta_c/2\theta)^4 \quad (\theta_c \ll \theta \ll 1). \tag{A3}$$

In the context of the first Born approximation (neglecting multiple scattering, thus "far" from the critical angle for total reflection), the effect of a nonstep interface profile is given by:[57–59]

$$R(Q_z) \approx \left(\frac{Q_c}{2Q_z}\right)^4 \left| \int dz e^{iQ_z z} \frac{1}{\rho_0}\frac{\partial\rho(z)}{\partial z} \right|^2 \quad (Q_z \gg Q_c), \tag{A4}$$

with $\rho_0 \equiv \rho(-\infty)$ and $Q_z = (4\pi/\lambda)\sin\theta$. The "Fresnel" reflectivity of the ideal silicon interface is modulated by the absolute-value squared of the Fourier transform of the derivative of the real surface density profile, yielding a series of Kiessig fringes[60,61] for a thin surface layer. For a stratified interface, described by the sum of error-function profiles between "slabs" of constant density, the Fourier transform yields a sum of Gaussians modulating the overall Q^{-4} dependence.

Alternately, the reflectivity can be calculated efficiently by using the matrix transfer multiplication method[62] taking into account interfacial widths.[63] This has the advantage of remaining valid near the critical angle. (Note, however, that x-ray beam coherence effects can be observed very close to the critical angle when using a synchrotron wiggler or undulator source.)

As the reflectivity depends both on incidence angle and on wavelength, different schemes can be employed, each presenting specific advantages, mostly technical, depending on the experimental conditions. Figure 14(a) shows schematically the wavevector transfer kinematics of a fixed-energy experiment where the angle of incidence is varied; Fig. 14(b) shows the corresponding wavevector transfer in a fixed-angle experiment where the x-ray beam energy is varied. This second scheme is of standard use for neutron time-of-flight reflectivity measurements, and an example of a composite spectrum taken at eight different, fixed incident angles is shown in Fig. 6. Both schemes were employed in this study.

2. Instrumental resolution

In a real experiment, the instrumental resolution reciprocal-space (three dimensional) volume is determined by incident and detected beam divergences as well as by the wavelength or energy resolution [see Fig. 14(c)]. The intensity measured is not purely specular: Diffuse scattering, both from the volume of the substrate or the surrounding environment and from surface roughness (nonplanar morphology of the surface), contributes to the measured signal. This is an often-overlooked, nontrivial problem[64] to be addressed through the careful design of the experiments and data analysis. In the present problem, whereas the diffuse scattering due to penetration to the bulk of the single-crystal silicon substrate is minimal, the diffuse scattering due to density fluctuations in the aqueous environment is, however, significant.

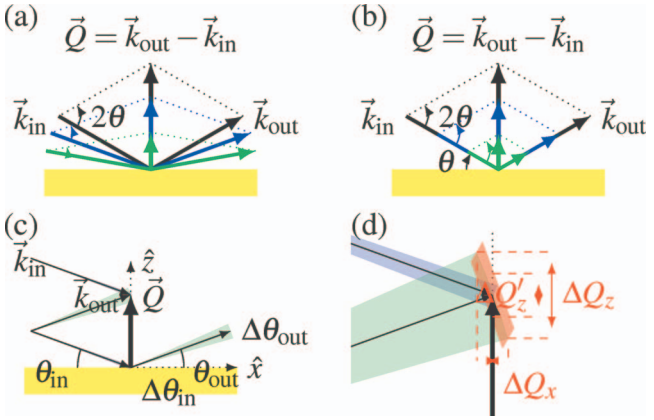

FIG. 14. (Color) Schematic construction of the wavevector transfer of specular reflectivity [$\vec{Q} = (4\pi/\lambda)\sin\theta\hat{z}$, $|\vec{k}_{in}| = |\vec{k}_{out}| = 2\pi/\lambda$, $\theta = \theta_{in} = \theta_{out}$]. (a) Fixed wavelength, variable angle of incidence and (b) fixed angle of incidence, variable wavelength. (c) The (blue/green) shaded regions schematize the incident/detector divergences $\Delta\theta_{in}$ and $\Delta\theta_{out}$, (d) Resolution volume around the scattering vector. The (red) region around $\vec{Q}$ shows a section of the convoluted resolution volume. $\Delta Q'_z = 2(2\pi/\lambda)\Delta\theta_{in}\cos\theta_{in}$, the *intersection* of this volume with the z axis, is the instrumental resolution for pure specular reflectivity and is independent of the angular resolution of the detector; $\Delta Q_z = (2\pi/\lambda)\Delta\theta_{out}\cos\theta_{out}$ is the *projection* of the extended volume with this axis and corresponds to the full width at half maximum of the Q_z resolution for the diffuse scattering around the specular axis; $\Delta Q_x = (2\pi/\lambda)\Delta\theta_{out}\sin\theta_{out}$ is the corresponding projection perpendicular to this axis in the scattering plane yielding the in-plane resolution. The divergences in the third dimension, out of the incidence plane, are not shown for clarity.

The instrumental resolution for specular reflectivity ($\theta_{out} = \theta_{in}$) is independent of the detector arm slits,[64] as can be seen in Fig. 14(d): $\Delta Q'_z = 2(2\pi/\lambda)\Delta\theta_{in}\cos\theta_{in}$ for $\Delta\theta_{out} > \Delta\theta_{in}$. However, opening the detector arm slits increases the resolution volume and, thus, the sensitivity to diffuse scattering from bulk density fluctuations and from surface roughness. The resolution in the direction of the surface plane $\Delta Q_x = (2\pi/\lambda)\Delta\theta_{out}\sin\theta_{out}$ is very high; the in-plane coherence length $\lambda/(\Delta\theta_{out}\sin\theta_{out})$ ranged from 3 mm at the critical angle down to 92 μm at the highest measured angles of incidence.

The x-ray intensity incident on the sample was systematically measured before each data run through a "scan" of the detector arm with the sample slightly lowered (by 0.5 mm) so as not to intercept the incident beam, yet traversing the liquid buffer (direct beam in Fig. 15). The ideal, trapezoidal, two-slit function is observed to be convoluted with small-angle scattering from the slit edges. We introduce here a convenient analytical function that can be used to describe the profile of the instrumental resolution,

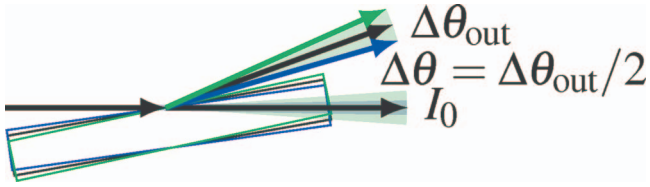

FIG. 15. (Color) Schema of the measurement of the direct-beam (with the sample lowered out of the figure) and rocking-curve profiles.

$$I(\theta_{out}) = \frac{I_0}{1 + \left(\frac{\theta_{out} - \theta_0}{\Delta\theta_{out}/2}\right)^p} + \text{background}. \quad \text{(A5)}$$

This empirical function varies from a Lorentzian form for $p=2$ to a squarelike function for higher values of this exponent (see Fig. 16). The scattering from the edges of real slits depends highly on the quality of the beamline alignment; As this alignment varied from electron-beam refill to refill as well as from very small changes in mechanical stability of the entire beamline, the exact form of the measured resolution function (parameters I_0, $\Delta\theta_{out}$, and p) differed slightly for each measurement. Thus, we used the area under the curve, $A=2\pi I_0 \Delta\theta_{out}/p \sin p$, for the normalization of the measured reflectivities.

The diffuse scattering from thermal density fluctuations in the buffer solution is independent of any length scale and, therefore, constant with wavevector transfer. However, the resolution volume does vary with angle and this contribution to the "background" is not constant. In addition, the diffuse scattering from surface roughness is modulated along the z direction in the very same manner as the specular reflectivity.[65] It is, therefore, essential to attempt to separate surface-diffuse scattering contribution as well from the measured reflectivity signal. Two schemes that can be employed to this end are shown in Fig. 17. In the first scheme [figure 17(a)], a "rocking curve" is recorded for each angle of incidence to be measured, the width of which should be exactly

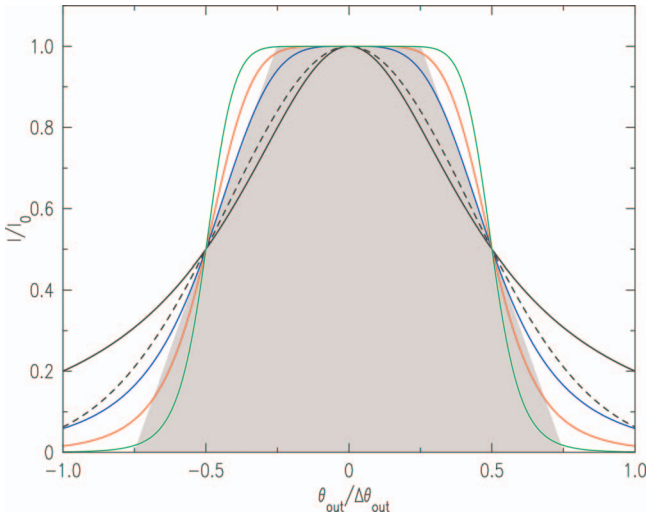

FIG. 16. (Color) Resolution function. Dashed line: Gaussian, solid lines: Eq. (A5)-("softest" to sharpest), black: $p=2$ (Lorentzian), blue: $p=4$, red: $p=6$, green: $p=10$, and gray: Ideal trapezoidal slit function with $\Delta\theta_{out}=2\Delta\theta_{in}$.

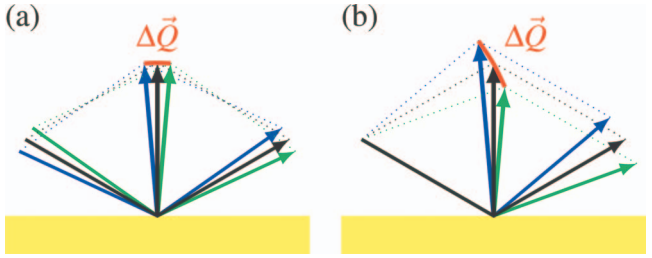

FIG. 17. (Color) Kinematics of a (a) "rocking curve" ($\theta_{in}+\theta_{out}=$constant) and (b) "detector scan" ($\theta_{in}=$constant). $\vec{Q}=(2\pi/\lambda)[(\cos\theta_{out}-\cos\theta_{in})\hat{x} + (\sin\theta_{out}+\sin\theta_{in})\hat{z}]$.

half that of the measured direct-beam profile (see Fig. 15). The second scheme [Fig. 17(b)] is more commonly used. However, this "detector scan" makes a sloping cut through reciprocal space and this can, in fact, lead to a poor estimation of the diffuse scattering contribution.

Figure 18 illustrates a real measurement of a series of rocking curves around the specular reflection. The advantages of this scheme for the determination of diffuse scattering and background subtraction are manyfold:

- First, and most importantly, this approach permits the use of a tight resolution configuration, in particular, a minimal detector slit gap (see Fig. 14) with the advantage of minimizing the sensitivity to diffuse scattering (the resolution function for specular reflectivity depends on the incident beam dimension in the incidence plane, whereas the resolution for diffuse scattering is dominated by the dimension of the detector-arm slits in this plane). Small variations in the condition for specular reflectivity (due to the extremely high mechanical positioning precision required) can be compensated in the analysis of the rocking curves, necessary under such

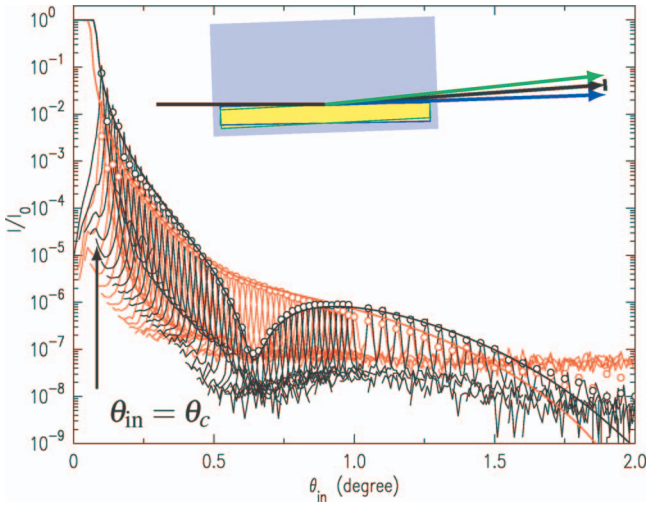

FIG. 18. (Color) Measured rocking curves ($\theta_{in}+\theta_{out}=2\theta$) for the acid-terminated sample in air (black) and under buffer solution (red). The background scattering (as seen in the lower envelope of the scans), modulated as for the specular reflectivity, arises from the surface roughness. Under buffer, this background is constant ($\sim 4\times10^{-8} I_0$) except for very grazing angles of incidence and is due to diffuse scattering from density fluctuations in the aqueous solution. Notice the anomalous surface reflections or Yoneda (Ref. 66) peaks (arrow) around $\theta_{in}=\theta_c$ (and $\theta_{out}=\theta_c$ by reciprocity).

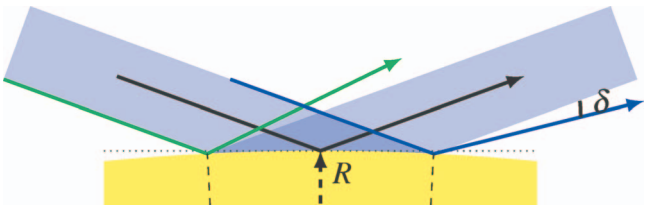

FIG. 19. (Color) Schema of the spreading upon reflection by a curved surface. The beam footprint is $h/\sin\theta$, where h is the beam height. The spreading angle, $\delta=4\sin^{-1}[h/(2R\sin\theta)]$, where R is the radius of curvature, is a function of this footprint and, thus, would decrease with increasing incidence angle.

tight resolution conditions (even for the very best diffractometers under near-perfect alignment).

- As the diffuse scattering from the surface structure is also modulated with Kiessig fringes as for the specular reflectivity, other schemes for background subtraction, in particular, scans of the detector angle for a fixed incidence angle, can lead to an incorrect estimation of the diffuse scattering contribution. This effect is most pronounced in the case of "tight" Kiessig fringes arising from a thick surface layer, indeed, catastrophic in the case of reflectivity measurements from metallic multilayers[67,68] (for example, under conditions of a minimum in the specular reflectivity fringe, a scan of the detector angle would measure adjacent peaks in the diffuse scattering at slightly higher and lower scattering wavevectors).
- A broadening of the reflected beam profile arising from an even slightly curved sample (see Fig. 19) can be detected and eventually compensated, as was necessary in the present study. Such a situation of a curved reflecting surface is particularly inevitable in the study of the air/liquid or liquid/liquid interfaces, even when the sample size is taken to be much larger than the capillary length. Of course, this broadening of the reflected beam profile can be and is usually compensated through a relaxation of the detector slit resolution, thus leading to an increased contribution of diffuse scattering to the measured signal.
- Finally, the counting statistics can be optimized through the scheme of measurement of rocking curves. For a good instrument with minimum overhead in the movement and counting operations, there is no time penalty in systematic measurement of reflectivity through the use of rocking curves.

[1] C. E. Hall and M. Litt, J. Biophys. Biochem. Cytol. **4**, 1 (1958).
[2] M. Beer, J. Mol. Biol. **3**, 263 (1961).
[3] D. Lang, A. K. Kleinschmidt, R. K. Zahn, and U. M. von W. Hellmann, Biochim. Biophys. Acta **88**, 142 (1964).
[4] D. Lang, H. Bujard, B. Wolff, and D. Russell, J. Mol. Biol. **23**, 163 (1967).
[5] M. Joanicot and B. Revet, Biopolymers **26**, 315 (1987).
[6] T. P. Beebe, T. E. Wilson, D. F. Ogletree, J. E. Katz, R. Balhorn, M. B. Salmeron, and W. J. Siekhaus, Science **243**, 370 (1989).
[7] R. J. Driscoll, M. G. Youngquist, and J. D. Baldeschwieler, Nature (London) **346**, 294 (1990).
[8] P. Wagner, S. Nock, J. A. Spudich, W. D. Volkmuth, S. Chu, R. L. Cicero, C. P. Wade, M. R. Linford, and C. E. Chidsey, J. Struct. Biol. **119**, 189 (1997).
[9] S. N. Patole, A. R. Pike, B. A. Connolly, B. R. Horrocks, and A. Houlton, Langmuir **19**, 5457 (2003).
[10] H. G. Hansma, R. L. Sinsheimer, M. Q. Li, and P. K. Hansma, Nucleic Acids Res. **20**, 3585 (1992).
[11] H. G. Hansma, J. Vesenka, C. Siegerist, G. Kelderman, H. Morrett, R. L. Sinsheimer, V. Elings, C. Bustamante, and P. K. Hansma, Science **256**, 1180 (1992).
[12] C. Rivetti, M. Guthold, and C. Bustamante, J. Mol. Biol. **264**, 919 (1996).
[13] M. Q. Li, H. G. Hansma, J. Vesenka, G. Kelderman, and P. K. Hansma, J. Biomol. Struct. Dyn. **10**, 607 (1992).
[14] Y. L. Lyubchenko, A. A. Gall, L. S. Shlyakhtenko, R. E. Harrington, B. L. Jacobs, P. I. Oden, and S. M. Lindsay, J. Biomol. Struct. Dyn. **10**, 589 (1992).
[15] Y. Lyubchenko, L. Shlyakhtenko, R. Harrington, P. Oden, and S. Lindsay, Proc. Natl. Acad. Sci. U.S.A. **90**, 2137 (1993).
[16] Y. L. Lyubchenko and L. S. Shlyakhtenko, Proc. Natl. Acad. Sci. U.S.A. **94**, 496 (1997).
[17] J. Yang, K. Takeyasu, and Z. Shao, FEBS Lett. **301**, 173 (1992).
[18] H. Schott, *Affinity Chromatography. Template Chromatography of Nucleic Acids and Proteins*, Chromatographic Science Vol. 27 (Marcel Dekker, New York, 1984).
[19] G. M. Church and S. Kieffer-Higgins, Science **240**, 185 (1988).
[20] M. Schena, D. Shalon, R. W. Davis, and P. O. Brown, Science **270**, 467 (1995).
[21] D. Shalon, S. J. Smith, and P. O. Brown, Genome Res. **6**, 639 (1996).
[22] E. Southern, K. Mir, and M. Shchepinov, Nature Genetics **21**, 5 (1999).
[23] D. Rhodes and A. Klug, Nature (London) **286**, 573 (1980).
[24] G. Adam and M. Delbrück, *Structural Chemistry and Molecular Biology*, edited by A. Rich and N. Davidson (Freeman, San Francisco, 1968), pp. 198–215.
[25] A. Goldar and J.-L. Sikorav, Eur. Phys. J. E **14**, 211 (2004).
[26] T. M. Squires and S. R. Quake, Rev. Mod. Phys. **77**, 977 (2005).
[27] J. M. Buriak, Chem. Rev. (Washington, D.C.) **102**, 1271 (2002).
[28] The Si(111) 4 in. wafers, 500–550 μm thick, n-doped (resistance of $5-10\ \Omega\,\mathrm{cm}\rightarrow(4-9)\times10^{14}\ \mathrm{P/cm^3}$), and polished on one side, were obtained from Siltronix, France.
[29] P. Allongue, C. Henry de Villeneuve, S. Morin, R. Boukherroub, and D. D. M. Wayne, Electrochim. Acta **45**, 4591 (2000).
[30] M. L. Munford, R. Cortès, and P. Allongue, Sens. Mater. **13**, 259 (2001).
[31] X.-S. Wang, J. L. Goldberg, N. C. Bartelt, T. L. Einstein, and E. D. Williams, Phys. Rev. Lett. **65**, 2430 (1990).
[32] As the chemical etching leaves a hydrogen-terminated silicon surface, here, there is no surface reconstruction of the silicon lattice.
[33] C. Douarche, Ph.D. thesis, Université de Lille 1-USTL, 2007.
[34] C. Douarche, J.-L. Sikorav, and A. Goldar, Biophys. J. **94**, 134 (2007).
[35] A. B. Sieval, A. L. Demirel, J. W. M. Nissink, M. R. Linford, J. H. van der Maas, W. H. de Jeu, H. Zuilhof, and E. J. R. Sudholter, Langmuir **14**, 1759 (1998).
[36] S. J. Roser, R. Felici, and A. Eaglesham, Langmuir **10**, 3853 (1994).
[37] R. Felici, Rigaku J. **12**, 11 (1995).
[38] See: http://www.esrf.eu/UsersAndScience/Experiments/SCMatter/ID10B/
[39] The grafted molecular layer can be viewed as a monolayer of dodecanoic acid where the terminal methyl group is here replaced by a surface silicon atom of the monocrystalline substrate: $Si(CH_2)_{10}COOH$.
[40] A. Faucheux, A. C. Gouget-Laemmel, C. Henry de Villeneuve, R. Boukherroub, F. Ozanam, P. Allongue, and J. N. Chazalviel, Langmuir **22**, 153 (2006).
[41] S. Marčelja, Biochim. Biophys. Acta **367**, 165 (1974).
[42] B. Deloche and J. Charvolin, J. Phys. (Paris) **37**, 1497 (1976).
[43] V. M. Kaganer, H. Mohwald, and P. Dutta, Rev. Mod. Phys. **71**, 779 (1999).
[44] G. Cohen and H. Eisenberg, Biopolymers **6**, 1077 (1968).
[45] C. G. Baumann, S. B. Smith, V. A. Bloomfield, and C. Bustamante, Proc. Natl. Acad. Sci. U.S.A. **94**, 6185 (1997).
[46] C. Frontali, E. Dore, A. Ferrauto, E. Gratton, A. Bettini, M. R. Pozzan, and E. Valdevit, Biopolymers **18**, 1353 (1979).
[47] C. Rivetti, C. Walker, and C. Bustamante, J. Mol. Biol. **280**, 41 (1998).
[48] A. F. H. Ward and L. Tordai, J. Chem. Phys. **14**, 453 (1946).
[49] D. Lang and P. Coates, J. Mol. Biol. **36**, 137 (1968).
[50] M. A. Frommer and I. R. Miller, J. Phys. Chem. **72**, 2862 (1968).
[51] A. Fick, London, Edinburgh Dublin Philos. Mag. J. Sci. **10**, 30 (1855).

[52] A. G. Frutos, Q. H. Liu, A. J. Thiel, A. M. W. Sanner, A. E. Condon, L. M. Smith, and R. M. Corn, Nucleic Acids Res. **25**, 4748 (1997).
[53] T. Strother, W. Cai, X. S. Zhao, R. J. Hamers, and L. M. Smith, J. Am. Chem. Soc. **122**, 1205 (2000).
[54] C. Fradin, A. Braslau, D. Luzet, M. Alba, C. Gourier, J. Daillant, G. Grubel, G. Vignaud, J. F. Legrand, J. Lal, J. M. Petit, and F. Rieutord, Physica B **248**, 310 (1998).
[55] C. Symietz, M. Schneider, G. Brezesinski, and H. Mohwald, Macromolecules **37**, 3865 (2004).
[56] The energy-dispersive core-electron screening correction $\Delta f'$ is very small for the light elements (0.1 for Si at 17.4 keV) and can be neglected here.
[57] P. Beckmann and A. Spizzichino, *The Scattering of Electromagnetic Waves from Rough Surfaces* (Macmillan, London, 1963).
[58] E. S. Wu and W. W. Webb, Phys. Rev. A **8**, 2065 (1973).
[59] A. Braslau, P. S. Pershan, G. Swislow, B. M. Ocko, and J. Als-Nielsen, Phys. Rev. A **38**, 2457 (1988).
[60] H. Kiessig, Ann. Phys. **402**, 715 (1931).
[61] H. Kiessig, Ann. Phys. **402**, 769 (1931).
[62] F. Abelès, Ann. Phys. (Paris) **3**, 504 (1948).
[63] L. Nevot and P. Croce, Rev. Phys. Appl. **15**, 761 (1980).
[64] P. S. Pershan, A. Braslau, A. H. Weiss, and J. Als-Nielsen, Phys. Rev. A **35**, 4800 (1987).
[65] J. Daillant, E. Bellet-Amalric, A. Braslau, T. Charitat, G. Fragneto, F. Graner, S. Mora, F. Rieutord, and B. Stidder, Proc. Natl. Acad. Sci. U.S.A. **102**, 11639 (2005).
[66] Y. Yoneda, Phys. Rev. **131**, 2010 (1963).
[67] R. Leguay, A. Dunlop, F. Dunstetter, N. Lorenzelli, A. Braslau, F. Bridou, J. Corno, B. Pardo, C. Colliex, A. Menelle, J. L. Rouviere, and J. Chevallier, Nucl. Instrum. Methods Phys. Res. B **106**, 28 (1995).
[68] R. Leguay, A. Dunlop, F. Dunstetter, N. Lorenzelli, A. Braslau, F. Bridou, J. Corno, B. Pardo, J. Chevallier, C. Colliex, A. Menelle, J. L. Rouviere, and L. Tome, Nucl. Instrum. Methods Phys. Res. B **122**, 481 (1997).
[69] B. E. Warren, Phys. Rev. **44**, 969 (1933).
[70] N. K. Adam, *The Physics and Chemistry of Surfaces*, 3rd ed. (Oxford University Press, London, 1941).
[71] A. Müller, Proc. R. Soc. London, Ser. A **120**, 437 (1928).